

Article

# Evidence of a Large Refrigerant Capacity in Nb-Modified $\text{La}_{1.4}\text{Sr}_{1.6}\text{Mn}_{2-x}\text{Nb}_x\text{O}_7$ ( $0.0 \leq x \leq 0.15$ ) Layered Perovskites

Akshay Kumar<sup>1</sup>, Jong Woo Kim<sup>2</sup>, Mohit K. Sharma<sup>1</sup> , Kavita Kumari<sup>1</sup>, Ankush Vij<sup>3</sup> and Bon Heun Koo<sup>1,\*</sup> <sup>1</sup> School of Material Science and Engineering, Changwon National University, Changwon 51140, Gyeongnam, Republic of Korea<sup>2</sup> Department of Functional Ceramics, Korea Institute of Materials Science (KIMS), Changwon 51508, Gyeongnam, Republic of Korea<sup>3</sup> Department of Physics & Astrophysics, Central University of Haryana, Jant-Pali, Mahendergarh 123031, India

\* Correspondence: bhkoo@changwon.ac.kr

**Abstract:** In this work, evidence of isothermal magnetic entropy change ( $\Delta S_M$ ) over a broad temperature region is presented in a series of  $\text{La}_{1.4}\text{Sr}_{1.6}\text{Mn}_{2-x}\text{Nb}_x\text{O}_7$  Ruddlesden–Popper compounds with niobium modification (Nb) ( $0.0 \leq x \leq 0.15$ ) at the manganese (Mn) site. The ceramic samples were obtained through a solid-state sintering method in optimized conditions. All compounds predominantly possessed Ruddlesden–Popper phase while a few additional reflections were resolved in Nb-doped compounds which indicates the separation of structural phases. These peaks are assigned to a separate layered perovskite and single perovskite with tetragonal symmetry and hexagonal symmetry, respectively. The microstructure of the pure sample reveals uniform grain morphology but in Nb-doped specimens chiefly three types of grains were found. It was assumed that the inter-connected large particles were of R-P phase which is dominant in both parent and  $x = 0.05$  compounds, while the hexagonal and polygonal morphology of grains in higher concentrations of dopants directly corroborates with the symmetry of single perovskite and additional layered perovskite phases, respectively. The parent compound exhibits a single  $\Delta S_M$  curve, whereas all Nb-substituted samples display bifurcated  $\Delta S_M$  curves. This indicated two transition regions with multiple magnetic components, attributed to distinct structural phases. The highest  $\Delta S_M$  values obtained for components corresponding to the R-P phase are  $2.32 \text{ Jkg}^{-1}\text{k}^{-1}$ ,  $0.75 \text{ Jkg}^{-1}\text{k}^{-1}$ ,  $0.58 \text{ Jkg}^{-1}\text{k}^{-1}$  and  $0.43 \text{ Jkg}^{-1}\text{k}^{-1}$  and for the second component located around room temperature are  $0.0 \text{ Jkg}^{-1}\text{k}^{-1}$ ,  $0.2 \text{ Jkg}^{-1}\text{k}^{-1}$ ,  $0.28 \text{ Jkg}^{-1}\text{k}^{-1}$  and  $0.35 \text{ Jkg}^{-1}\text{k}^{-1}$  for  $x = 0.0, 0.05, 0.10$  and  $0.15$  compositions, respectively, at 2.5 T. Due to the collective participation of both components the  $\Delta S_M$  was expanded through a broad temperature range upon Nb doping.

**Keywords:** Ruddlesden–Popper phase; isothermal magnetic entropy change; phase separation; magnetocaloric effects; solid-state sintering



**Citation:** Kumar, A.; Kim, J.W.; Sharma, M.K.; Kumari, K.; Vij, A.; Koo, B.H. Evidence of a Large Refrigerant Capacity in Nb-Modified  $\text{La}_{1.4}\text{Sr}_{1.6}\text{Mn}_{2-x}\text{Nb}_x\text{O}_7$  ( $0.0 \leq x \leq 0.15$ ) Layered Perovskites. *Magnetochemistry* **2024**, *10*, 22.

<https://doi.org/10.3390/magnetochemistry10040022>

Academic Editor: Lotfi Bessais

Received: 28 February 2024

Revised: 27 March 2024

Accepted: 29 March 2024

Published: 29 March 2024



**Copyright:** © 2024 by the authors. Licensee MDPI, Basel, Switzerland. This article is an open access article distributed under the terms and conditions of the Creative Commons Attribution (CC BY) license (<https://creativecommons.org/licenses/by/4.0/>).

## 1. Introduction

In the pursuit of efficient and eco-friendly cooling technologies, magnetic refrigeration has emerged as a promising alternative to conventional vapor compression refrigeration methods. The magnetocaloric effect (MCE), which involves the adiabatic temperature change in a magnetic material subjected to an external magnetic field, lies at the heart of magnetic refrigeration technology [1–3]. Among various magnetic materials, transition metal oxides, particularly perovskites, have drawn significant attention for their remarkable magnetocaloric properties and potential for practical applications [4–6]. One class of perovskites, the Ruddlesden–Popper (R-P) phases, has recently gained prominence in the field of magnetocaloric research due to their unique double layer crystal structure and tunable magnetic properties [7–9]. In particular, the  $\text{La}_{1.4}\text{Sr}_{1.6}\text{Mn}_2\text{O}_7$  perovskite has shown significant promise for magnetocaloric applications owing to its metamagnetization,

Curie temperature near room temperature and table like entropy change [10,11]. These magnetic characteristics of manganites primarily arise from the presence of a mixed-valence state involving both  $Mn^{3+}$  and  $Mn^{4+}$  ions. This mixture results in ferromagnetic (FM) ordering from  $Mn^{3+}$ -O- $Mn^{4+}$  double exchange interactions and antiferromagnetic (AFM) ordering from superexchange interactions between  $Mn^{3+}$  ions [12,13]. To further enhance its magnetocaloric performance, doping strategies have been explored, and one such intriguing avenue is the element substitution at the manganese (Mn) site [14,15], secondly, by using sophisticated preparation methods. From the structural perspective, substituting Mn with an element having different ionic radii causes a change in the unit cell volume and lattice constants, eventually above a certain threshold the element substitution alters the crystal structure and affects its symmetry. This may lead to distortions in the crystal lattice, influencing the magnetic and transport properties of the manganite perovskites [16–18]. Moreover, there are reports that suggest modification at the Mn site with Nb, Ni or Fe ions could promote change in the crystal phases, such as rhombohedral, orthorhombic or cubic phases, and influence the transition temperatures between these phases [19,20]. Furthermore, the magnetic properties of manganite perovskites are mainly determined by the magnetic ordering of Mn ions, hence, a modification at the Mn site with a slightly higher or lower oxidation state ion is expected to alter the short- and long-range magnetic interactions, leading to changes in the magnetic ordering temperature ( $T_C$ ), magnetic transition width and the nature of the magnetic phase transitions [21]. In the context of MCE, the Mn-site substitution reportedly modifies the height and shape of the magnetic entropy curve [11], while it may also shift the  $T_C$ , hence, influencing the temperature range over which the magnetocaloric effect occurs [22]. Previous work on a few perovskite systems doped with transition metals have shown promising results. Nanto et al. [23] reported enhanced magnetocaloric properties in  $La_{0.7}Ca_{0.3}MnO_3$  through Niobium (Nb) doping, where a slight Nb doping produces a broad entropy change against a temperature span that surpassed the temperature span of the sample without Nb doping. Similarly, Santhosh et al. [7] investigated the role of Co doping in R-P perovskites that revealed an atomically disordered quasi-two-dimensional phase with short-range antiferromagnetic ordering around room temperature and frozen magnetic clusters at lower temperatures, and it produced a giant exchange anisotropy and a spin glass state. Magnetocaloric research on nominal compositions of  $La_{0.7}Sr_{0.3}MnO_3$  compounds upon the substitution of Fe, Ni, Cr and Cu metals at the Mn site revealed an improved refrigeration capacity over a wider operating temperature range [14,17,22,24]. Surprisingly, there is a large scarcity of MCE studies in Mn-modified R-P perovskite phases in the available literature. In these compounds, there are two layers of ferromagnetic metallic  $MnO_2$  placed side by side. These layers are separated by a rock-salt  $(La,Sr)_2O_2$  layer. This setup helps to maintain a pattern resembling two-dimensional networks of  $MnO_6$  octahedra and makes them a promising candidate for studying the layered magnetic interactions. In this context, our research article presents a comprehensive experimental investigation on the magnetocaloric properties of Nb-doped  $La_{1.4}Sr_{1.6}Mn_{2-x}Nb_xO_7$  perovskite with a specific focus on elucidating the influence of phase separation in double-layer perovskite. In general, Nb accommodates variable oxidation states with +5 being the most stable state as compared to Mn which stabilizes in 3+ and 4+, whereas the atomic radii of Nb is also slightly larger than Mn. Thus, the substitution of Nb at the Mn site is expected to induce lattice distortions, modify the long/short range magnetic interactions and thereby influence the magnetocaloric response of the material. By systematically varying the doping content (x) of Nb, we aim to elucidate the impact of Nb doping on the magnetocaloric effect, offering valuable insights into the underlying physics governing the observed phenomena.

## 2. Experiment and Characterization Methods

The  $La_{1.4}Sr_{1.6}Mn_{2-x}Nb_xO_7$  series with varying Nb content ( $0.0 \leq x \leq 0.15$ ) was synthesized through the ceramic sintering technique. Raw materials, namely  $La_2O_3$ ,  $Nb_2O_5$ , SrO and  $Mn_2O_3$  with a purity level of 99.9% from Sigma-Aldrich, were meticulously

weighed according to their stoichiometric proportions. These powders were then subjected to grinding before being placed into 250 mL ball-mill vials, accompanied by a small volume of ethanol. A consistent powder-to-ball ratio of 1:20 was maintained, employing zirconia balls of 5 mm in diameter. The ball-milling process was conducted for a duration of 20 h at a speed of 210 rpm. The homogenized slurry was transferred to evaporating dishes and subjected to drying at 70 °C within an oven. The resultant dried powders were subsequently ground and pressed into discs with dimensions of 2 mm thickness and 10 mm diameter, and then subjected to calcination at 1100 °C for 36 h within a muffle furnace. This calcination process was interspersed with intermediate pelletization and re-pelletization steps to enhance material homogeneity. Ultimately, the pellets underwent sintering at 1400 °C for 24 h, with a gradual cooling of the muffle furnace back to room temperature. The crystallographic phases of the obtained pellets were determined via X-ray diffraction (XRD) analysis using a PANalytical X'Pert Pro diffractometer equipped with a copper (Cu)  $K\alpha$  X-ray source. The unit cell constants and structural parameters were derived through the refinement of XRD patterns using the Rietveld procedure implemented in FullProf software (for windows 10 PC, <https://www.ill.eu/sites/fullprof/php/downloads.html>, accessed on 20 March 2024). The pseudo-Voigt function was employed for peak fitting and background was corrected with linear interpolation. Microstructural evaluation and elemental composition analysis of the sintered pellets were conducted utilizing a scanning electron microscope (SEM; Jeol-JSM-6510, JEOL Ltd., Tokyo, Japan) equipped with an energy-dispersive X-ray spectroscope (EDX). The magnetic response characteristics of the samples were assessed using a vibrating sample magnetometer (VSM) housed within a Physical Property Measurement System (PPMS; VersaLab by Quantum Design USA). All magnetic measurements were performed on cylindrical samples measuring  $2 \times 3$  mm, with the magnetic field applied in a parallel fashion to the axial orientation. Magnetization versus temperature (M-T) profiles were recorded employing a field-cool protocol, spanning a temperature range from 50 K to 400 K, with a controlled cooling–heating rate of 5 K/min and a 0.05 T magnetic field. Field-dependent mass magnetization (M-H) curves were acquired at various temperatures (isotherms), encompassing an applied magnetic field of up to 3 T.

### 3. Results and Discussion

The XRD profiles of the Nb doped series are shown in Figure 1a–d; all compounds possess Ruddlesden–Popper tetragonal phase with an  $I4/mmm$  space group symmetry [25,26]. The Rietveld refinement of XRD profiles revealed that with respect to the Nb concentration the unit cell constants (a, b) increased from 3.86357 Å for  $x = 0.0$  up to 3.87041 Å for the highest Nb concentration, which indicates an expansion in interplanar spacing and unit cell volume as is also evident from Table 1. This could occur when a higher ionic radii ion like Nb is incorporated into the lattice in place of smaller radii Mn [23,27]. A few additional diffraction peaks at  $2\theta$  positions 28.2°, 30.8° and 40.1° are observed in the XRD profiles of the Nb-doped specimens while remaining unresolved in the parent compound. The initial two peak positions are assigned to another layered perovskite with an  $I41/a$  tetragonal symmetry [28], whereas the later one is designated to single perovskite consisting of a hexagonal R-3C symmetry which often appears alongside the R-P phase [29,30]. The intensity of these peaks rises with respect to the Nb content, indicating an increase in the fraction of each phase which is verified using the Rietveld refinement results supplied in Table 1. From these findings it is anticipated that Nb ions were partially incorporated into the lattice of each perovskite phase beside the R-P perovskite.

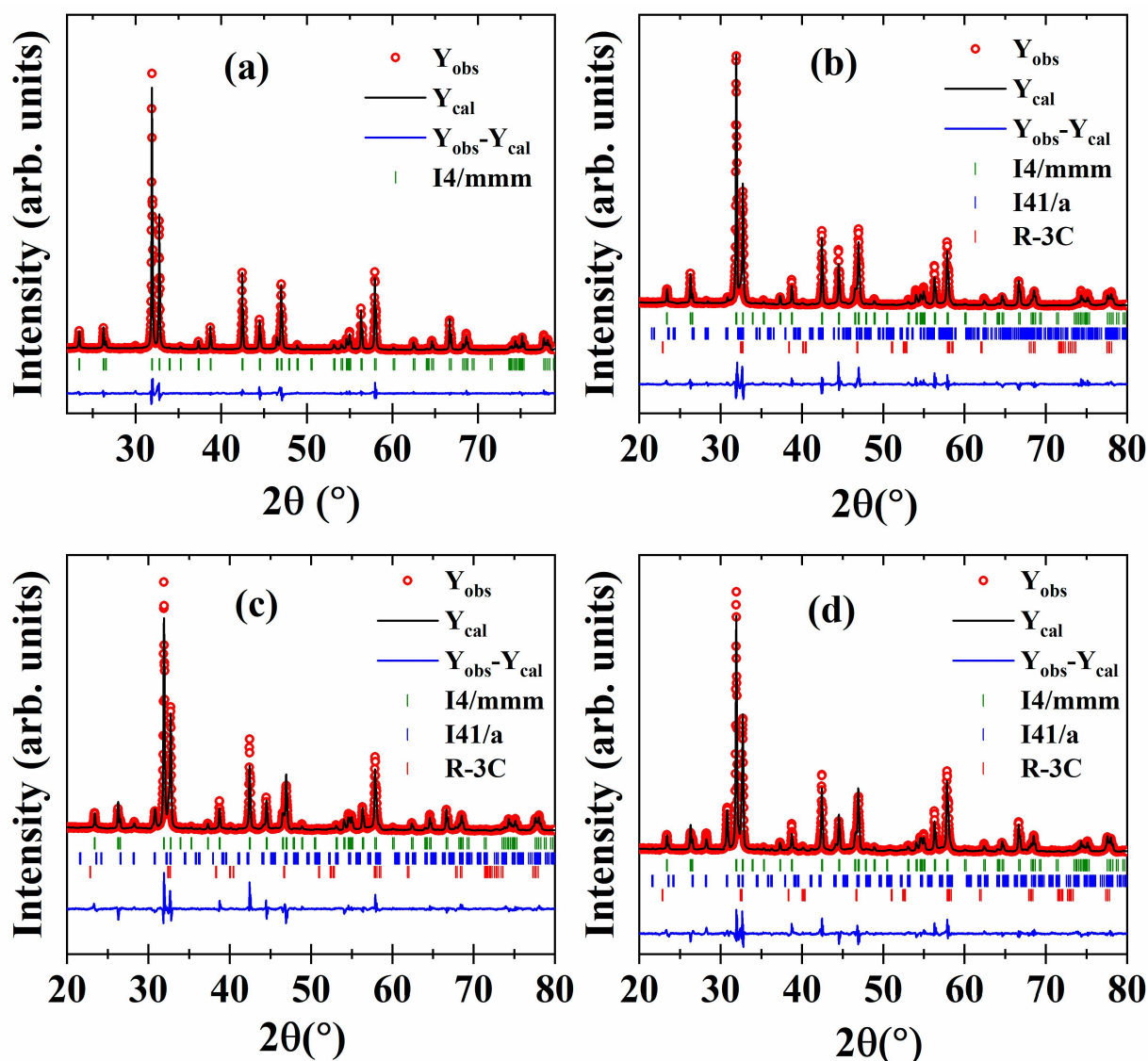


**Figure 1.** The room temperature XRD profiles refined using the Rietveld method for  $\text{La}_{1.4}\text{Sr}_{1.6}\text{Mn}_{2-x}\text{Nb}_x\text{O}_7$  series with varying Nb content such that (a)  $x = 0.0$ , (b)  $x = 0.05$ , (c)  $x = 0.10$  and (d)  $x = 0.15$ .

**Table 1.** Parameters derived from the Rietveld refinement of XRD patterns of the prepared  $\text{La}_{1.4}\text{Sr}_{1.6}\text{Mn}_{2-x}\text{Nb}_x\text{O}_7$  ( $0.0 \leq x \leq 0.15$ ) series.

Nb Concentration (x)	x = 0.0	x = 0.05	x = 0.1	x = 0.15
Space group = <i>I4/mmm</i>	x = 0.0	x = 0.05	x = 0.1	x = 0.15
Unit cell parameters (Å) a = b; ≠ c	3.86357 (2); 20.35096 (5)	3.86844 (3); 20.34060 (4)	3.86913 (3); 20.34580 (1)	3.87041 (2); 20.33350 (4)
Unit cell volume (Å <sup>3</sup> )	303.78296 (3)	304.393553 (2)	304.580013 (4)	304.597319 (2)
$\chi^2$	1.84	2.01	2.48	1.98
$R_{wp}$	10.1	12.6	13.4	11.7
$R_p$	9.8	11.9	12.8	11.2
$R_{exp}$	6.12	5.82	7.42	5.46
<i>I4/mmm</i> (R-P phase) (wt%)	100 (0.72)	89.26 (0.49)	79.73 (0.13)	72.71 (0.17)
R-3c (hexagonal perovskite phase) (wt%)	~	9.61 (0.55)	16.55 (0.83)	19.12 (0.27)
<i>I41/a</i> (tetragonal perovskite phase) (wt%)	~	1.13 (0.05)	3.72 (0.08)	8.17 (0.11)

In Figure 2, the microstructure of each specimen reveals an overall compact matrix with surprisingly large size grains, well-defined grain boundaries for the parent compound and a diminishing grain size upon Nb doping. A slightly high number of pores are visible in the undoped parent compound which tend to minimize for  $x = 0.05$  and vanish for higher concentrations of the dopants. In addition, the pure sample reveals uniform grain morphology but in the Nb-doped specimens chiefly three types of grains are foreseen: ones that are large in size, interconnected with the grain boundaries resembling the grains of the parent compound; the other two are comparatively very small in size, protrude out of the surface and are distributed in patches over the larger grains while acquiring a hexagonal and polygonal morphology. Such a contrast in the morphology of grains of Nb-doped compounds could be associated with the different perovskite phases. It is assumed that the interconnected large particles belong to the R-P phase which is dominant in both parent and  $x = 0.05$  compounds but declined in the specimens with high Nb content. Meanwhile, the hexagonal and polygonal morphology directly corroborates with the single perovskite and additional layered perovskite phase, respectively. The parted structural phases could plausibly have moved towards the material's surface through diffusion during the sintering process, as validated by observations in the micrographs. This phenomenon resonates with prior findings, wherein it was posited that the variation in the diffusion coefficients, reaction kinetics, and sintering temperatures among the distinct structural phases give rise to the precipitation phenomena on the surface of the pellets [31]. Consequently, it is reasonable to infer that the microstructure of the material is subject to the transformative influence of Nb doping because of the involvement of structural phase separation, and concurrently promoting the shrinkage of the average grain size and porosity.

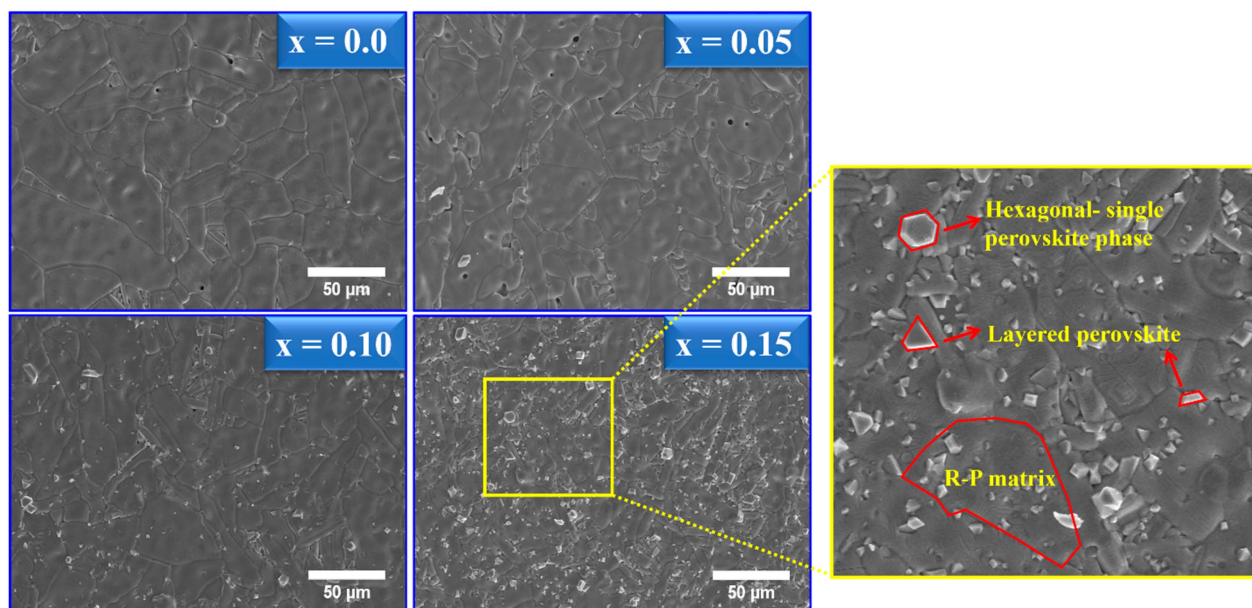


**Figure 2.** The SEM images of the surface of the microstructure are given with respect to the Nb concentrations. The magnified image on the right indicates the varied morphology of grains for the  $x = 0.15$  composition.

The magnetization response with respect to temperature is shown in Figure 3. It revealed an increase in magnetization upon decreasing the temperature that signifies ferromagnetic to paramagnetic (FM–PM) transition for all samples. Each sample represents two transition temperatures ( $T_C$ ), one below 100 K (transition 1) and the other located above room temperature (transition 2). These transition points individually represent the magnetic contribution of each structural phase for which the FM–PM transition in the low temperature region is allotted to the LSMO R-P phase [32], and  $T_C$  values towards

room temperature correspond to the other perovskite phase [30]. Upon Nb substitution, each of the transition points abruptly shifted towards the low temperature region from 80 K to 60 K and 370 K to 308 K, respectively. The decrease in  $T_C$  indicates destruction in long-range Mn-O-Mn magnetic ordering due to the incorporation of Nb in place of Mn which promotes short-range Mn-O-Nb, Nb-O-Nb magnetic interactions [23,33]. Surprisingly, the spontaneous magnetization is small in all the Nb-substituted compounds as compared to the undoped specimen. The decline in the magnetization value is ascribed to the destruction of ferromagnetic coupling in the sense that the anti-site  $Nb^{5+}$  ions destroyed the long-range double exchange  $Mn^{3+}$ -O- $Mn^{4+}$  interactions and promoted superexchange interactions through  $Nb^{5+}$ -O channels. In addition, it has been established in prior studies that the partial substitution of high oxidation state elements,  $Nb^{5+}$ -ions in place of the  $Mn^{3+}/Mn^{4+}$  site, naturally facilitates a vacancy in the lattice [23]; this may also destroy long-range ferromagnetic ordering. It is worth noting that among the Nb-doped compounds, the transition width of the first component decreases with an increase in the Nb concentration, while the contribution of the second component swiftly rises, and such type of magnetization behavior symbolizes a competition among the phase separated magnetic states. In the  $x = 0.15$  composition, the competing additional perovskite phase dominantly suppressed the R-P phase, hence, the magnetization corresponding to this component is revealed. In Figure 4a–d, the isothermal magnetization response of the Nb-doped series with respect to the external field (M-H) is presented within the temperature range of the FM–PM transition. Below the transition temperature, the magnetization value tends to rise linearly against the magnetic field values, achieving a plateau at a critical field and then progressing towards saturation, thereby validating the ferromagnetic behavior. Whereas the saturation point is neglected in Nb-doped compounds; it reclaimed the linear curve past the plateau which signifies the presence of magnetic clusters in the ferromagnetic domain. Interestingly, in these samples the ferromagnetic plateau in magnetization curves persists also beyond the first transition region ( $\geq 100$  K) and tends to diminish far above 300 K. This indicates that the ferromagnetic region of the competing second magnetic component coexists within the main domain of the first component, hence, it collectively reflects a ferromagnetic magnetization response within a broad temperature region. In this context, the M-H curves achieve a complete paramagnetic state above the transition temperature of the second component, as evident from M-H isotherms.

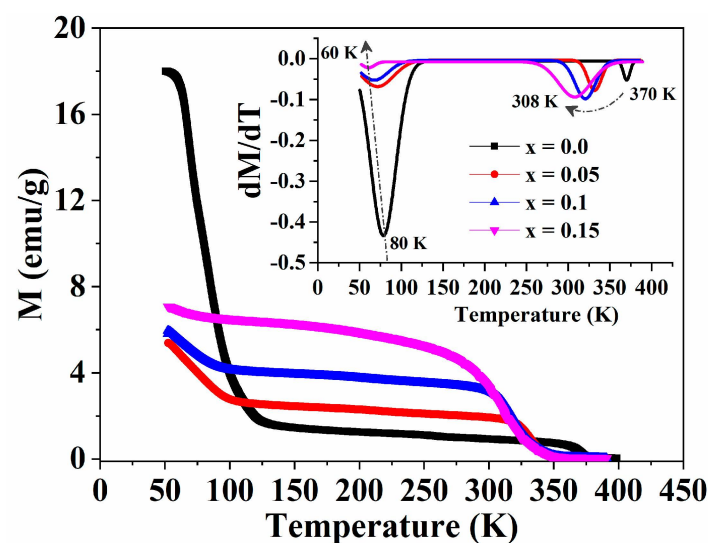


**Figure 3.** The thermomagnetic measurements of the  $La_{1.4}Sr_{1.6}Mn_{2-x}Nb_xO_7$  ( $0.0 \leq x \leq 0.15$ ) series, measured under 500 Oe magnetic field while cooling the samples from 400 K to 50 K. The corresponding  $dM/dT$  curves derived from the M-T data are given in the inset.

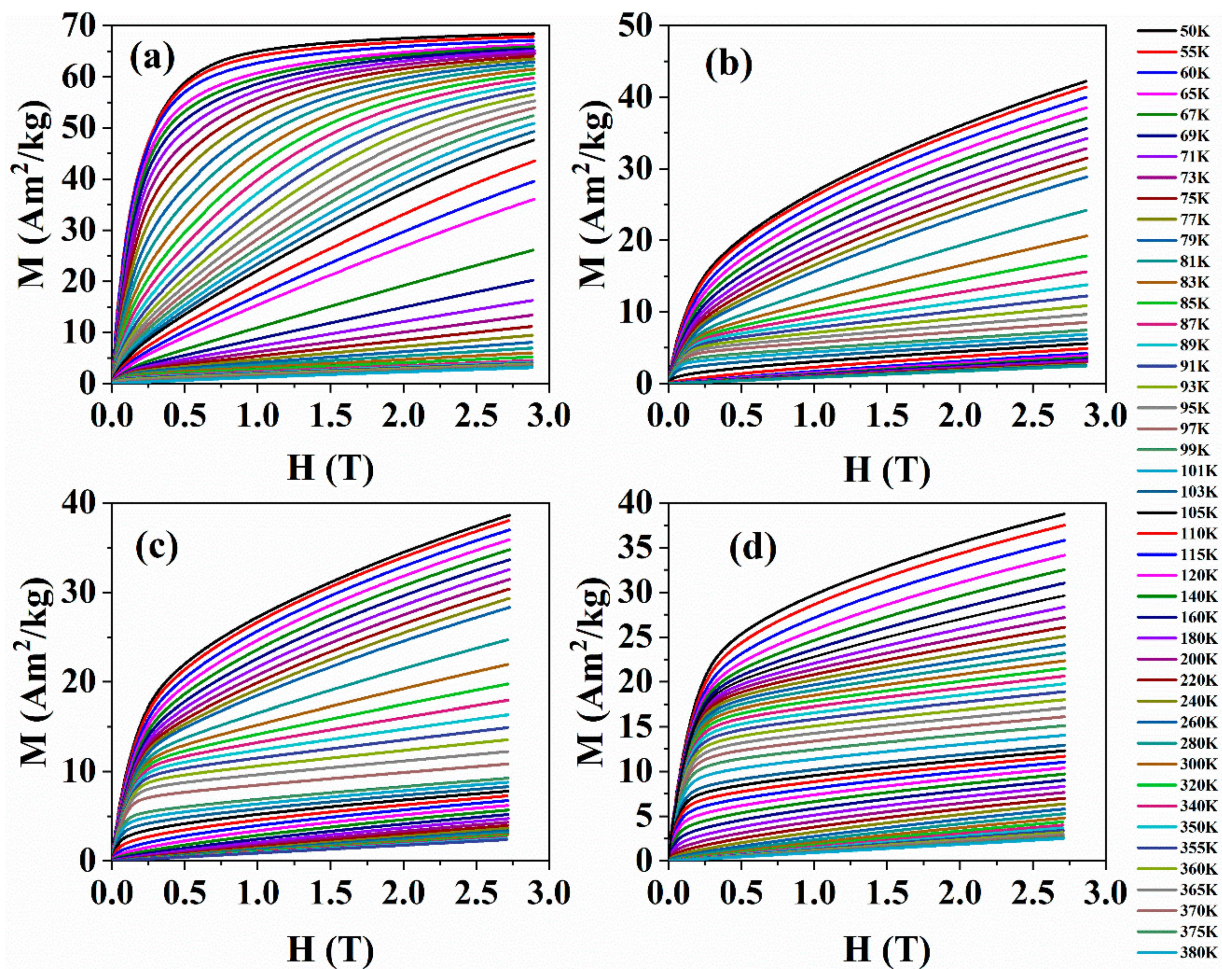


**Figure 4.** Isothermal mass magnetization curves measured against external magnetic field up to 3T at various temperature points for (a)  $x = 0.00$ , (b)  $x = 0.05$ , (c)  $x = 0.10$  and (d)  $x = 0.15$ , Nb concentrations.

Further, the isothermal magnetization curves were employed in constructing the Arrott plots to assess the nature of the magnetic transition. The  $M^2$  values of each isotherm are plotted against  $H/M$  as shown in Figure 5a–d. The Arrott curves reflect that the all samples contain mixed magnetic clusters such that in the transition region the  $M^2$  curves initially progress in a linear manner then rise abruptly in the high field region, thereby developing an S-shape curve against the  $H/M$  axis, which is also observed in other compounds reported elsewhere [11]. Moreover, according to the Banerjee criteria [34], the Arrott curves of each sample are deemed to possess an overall positive slope of  $M^2$  against the  $H/M$  axis, thereby pointing towards a second order magnetic transition. However, we face challenges in extracting the slope from the Arrott curves in Nb-doped compositions due to presence of the mixed magnetic components, therefore, the slope for each magnetic component in the respective transition region was calculated independently. As expected, a positive slope for each component is identified thereby validating the second order magnetic phase transition in the conjunction of phase separated magnetic states. The second order magnetic phase transition of these magnetic compounds is very attractive for magnetocaloric application in order to compensate for the magneto-thermal losses.

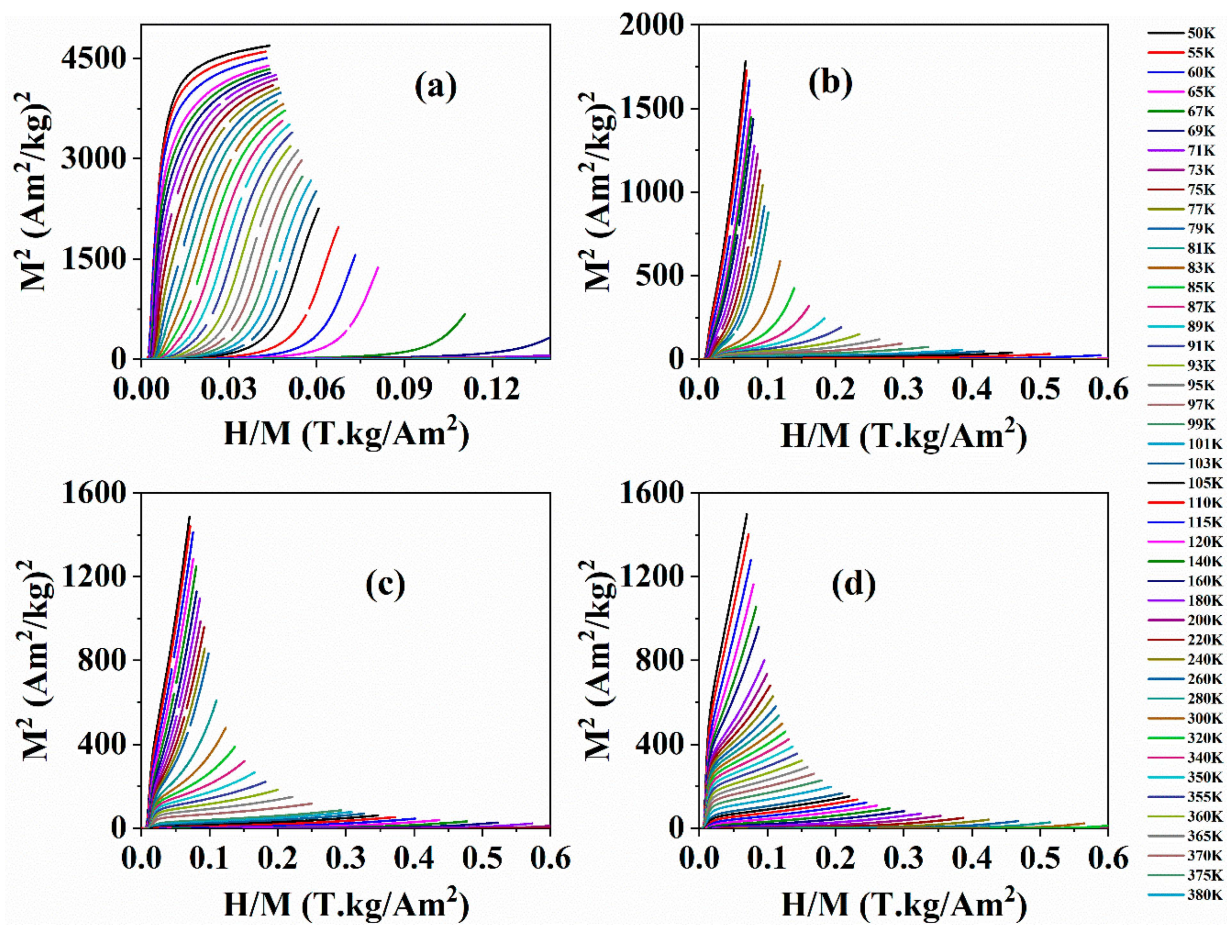


**Figure 5.** The respective Arrott plots derived from isothermal magnetization curves of  $\text{La}_{1.4}\text{Sr}_{1.6}\text{Mn}_{2-x}\text{Nb}_x\text{O}_7$  series, for which (a)  $x = 0.00$ , (b)  $x = 0.05$ , (c)  $x = 0.10$ , and (d)  $x = 0.15$ .

The magnetocaloric performance of the  $\text{La}_{1.4}\text{Sr}_{1.6}\text{Mn}_{2-x}\text{Nb}_x\text{O}_7$  series was analyzed through the change in magnetic entropy ( $\Delta S_M$ ). For this purpose, the Maxwell equations for a magnetic phase transition [35] were employed for the isothermal magnetization measurements, such that:

$$\Delta S_M(T, M) = S_M(T, H) - S_M(T, 0) = \int_0^H \left( \frac{\partial S}{\partial H} \right)_T dH = \int_0^H \left( \frac{\partial M}{\partial T} \right)_H dH \quad (1)$$

Equation (1) can be expressed as follows, considering discrete experimental values:

$$|\Delta S_M| = \sum \frac{M_i - M_{i+1}}{T_{i+1} - T_i} \Delta H_i \quad (2)$$

Here,  $M_i$ ,  $M_{i+1}$  are the incremental changes in isothermal magnetization corresponding to incremental changes at their respective measuring temperature steps  $T_{i+1}$ ,  $T_i$ , within the influence of an externally applied magnetic field, denoted as  $H_i$ . The acquired  $\Delta S_M$  curves at different magnetic fields against the temperature scale are given in Figure 6a–d. The parent compound disclosed a single curve at each value of the magnetic field, situated around the respective  $T_C$  of 80 K. The height of  $\Delta S_M$  curves ascended with the increase in the magnetic field value. This trend is sustained in all the compositions as expected for a magnetocaloric material. Moreover, the  $\Delta S_M$  curves split into two in all the Nb-substituted specimens, each peak representing the respective transition region of both magnetic components. The highest  $\Delta S_M$  values are obtained for the component corresponding to the R-P phase and have values of  $2.32 \text{ Jkg}^{-1}\text{k}^{-1}$ ,  $0.75 \text{ Jkg}^{-1}\text{k}^{-1}$ ,  $0.58 \text{ Jkg}^{-1}\text{k}^{-1}$  and  $0.43 \text{ Jkg}^{-1}\text{k}^{-1}$

for  $x = 0.0, 0.05, 0.10$  and  $0.15$  compositions, respectively, at 2.5 T. Likewise, for the second component, the maximum values of  $\Delta S_M$  are  $0.0 \text{ Jkg}^{-1}\text{k}^{-1}$ ,  $0.2 \text{ Jkg}^{-1}\text{k}^{-1}$ ,  $0.28 \text{ Jkg}^{-1}\text{k}^{-1}$  and  $0.35 \text{ Jkg}^{-1}\text{k}^{-1}$ . The decrease in entropy values of the first component and/or increase in second components simply suggests a competing nature of both separated magnetic components. Interestingly, the temperature span ( $\Delta T$ ) of the  $\Delta S_M$  curves of the first region is relatively narrower than the region located towards high temperatures. Due to the collective participation of both components, the entropy curves expanded through a broad temperature range upon Nb doping. The refrigerant capacity (RC) is another important parameter for evaluating the cooling/heating power of a magnetocaloric compound for practical use. The RC represents the extent of energy variation triggered by magnetic entropy across the complete operational temperature span. Herein the RC values were calculated using the entropy curves [36,37]:

$$RC = \int_{T_{Cold}}^{T_{Hot}} \Delta S_M dT \quad (3)$$

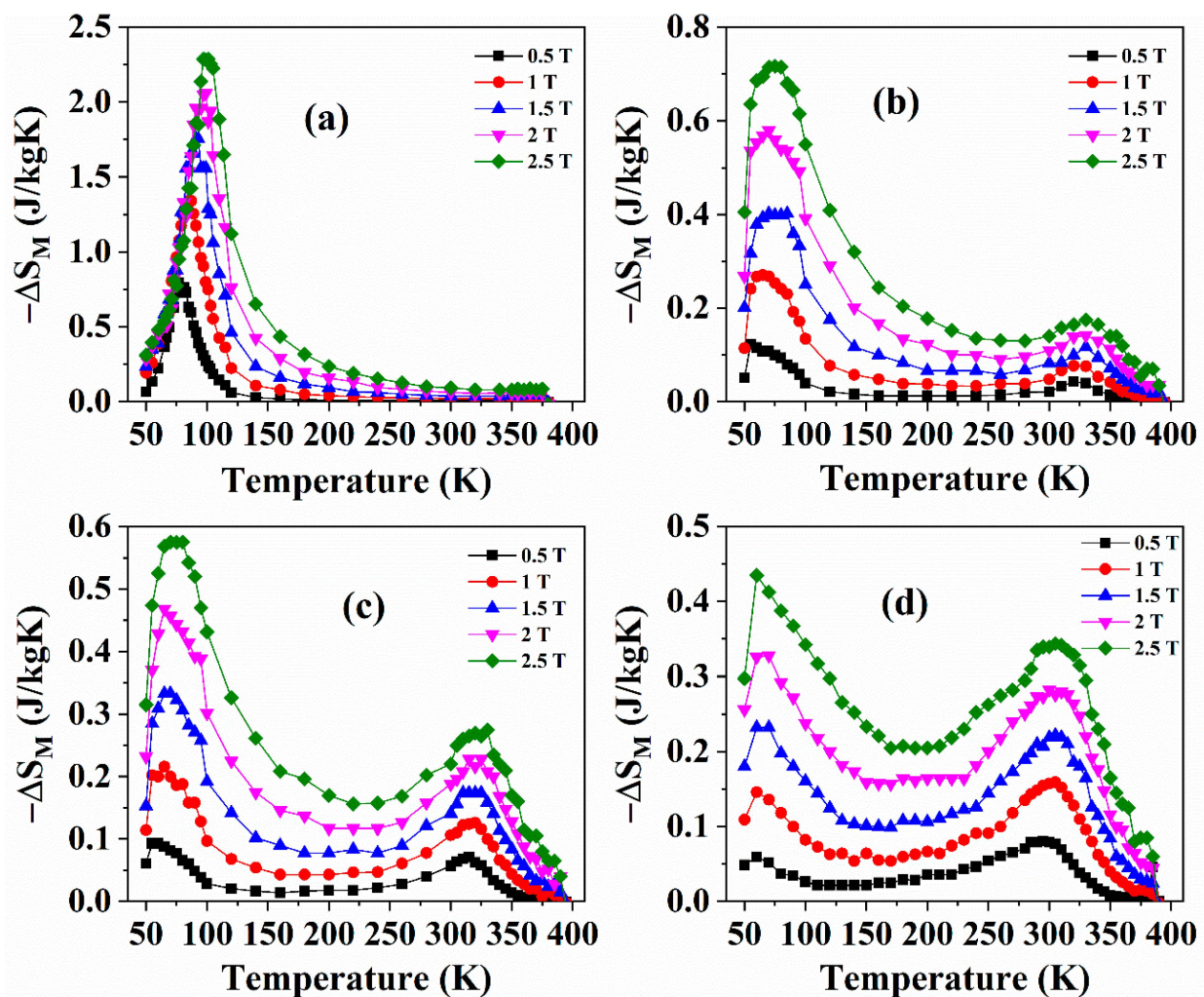


**Figure 6.** Isothermal entropy change vs. temperature curves given at various magnetic field strengths in  $\text{La}_{1.4}\text{Sr}_{1.6}\text{Mn}_{2-x}\text{Nb}_x\text{O}_7$  compounds, for which (a)  $x = 0.00$ , (b)  $x = 0.05$ , (c)  $x = 0.10$  and (d)  $x = 0.15$ .

Here,  $T_{Hot}$  and  $T_{Cold}$  correspond to the temperature points spanning the higher and lower ends of the full width at half maximum of the  $\Delta S_M$  curves. Since the undoped compound has a single  $\Delta S_M$  curve, the RC values are simply derived within the temperature points where the  $\Delta S_M$  value is half of the peak value which is found to be  $84 \text{ J/kg}$  for

the 2.5 T field. On the other hand, due to the dual  $\Delta S_M$  peaks in Nb-doped samples, the RC values were obtained by fitting both the peaks with the Gaussian function within the available temperature range and then adding individual RC values of each component (see Figure 7). The acquired values of RC at 2.5 T are 39 J/kg, 48 J/kg and 63 J/kg for  $x = 0.05$ , 0.10 and 0.15 Nb concentrations, respectively. The increase in RC value with Nb content is because of the rise in both  $\Delta S_M$  peaks over a broad temperature range. While the RC values of doped compounds are relatively smaller than those of the parent compound, what is particularly noteworthy is that the refrigerant capacity value obtained for Nb-doped compounds remains consistent across a wide temperature range. In contrast, the parent compound, despite its higher value, is sustained only up to a temperature region  $\leq 60$  K. A brief comparison with a few selected double perovskite compounds which are claimed to have a reasonable MC performance is provided in Table 2.

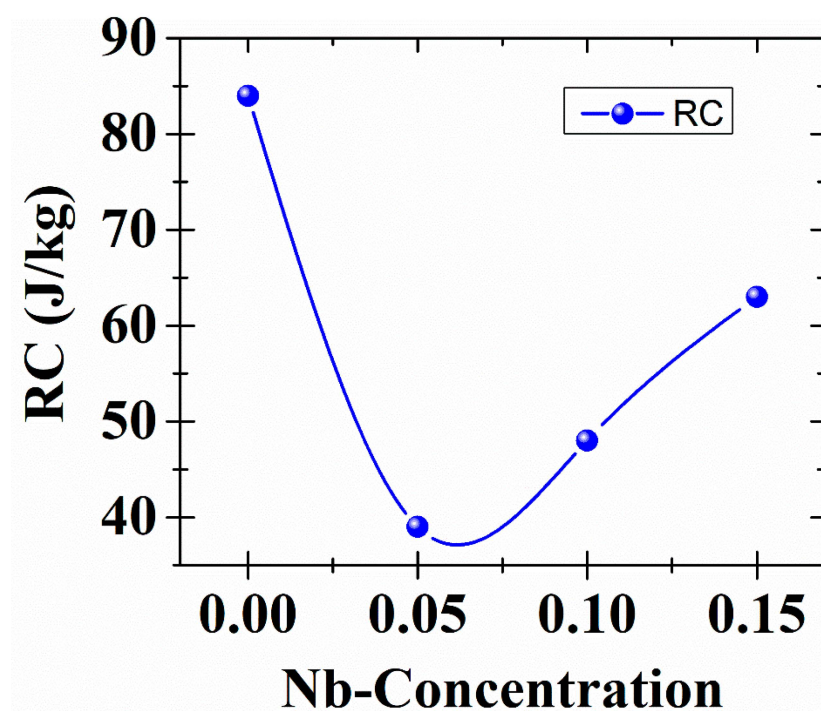


**Figure 7.** The obtained highest RC values for each specimen at an applied magnetic field of 2.5 T.

**Table 2.** Comparison of refrigerant capacity of compounds prepared in this work with other double perovskite compounds.

Compound Name	$T_C$ (K)	Magnetic Field (T)	RC (J/kg)	References
$\text{La}_{1.4}\text{Sr}_{1.6}\text{Mn}_2\text{O}_7$	80/370	2.5	84	Current work
$\text{La}_{1.4}\text{Sr}_{1.6}\text{Mn}_{1.95}\text{Nb}_{0.05}\text{O}_7$	66/320	2.5	39	Current work
$\text{La}_{1.4}\text{Sr}_{1.6}\text{Mn}_{1.85}\text{Nb}_{0.15}\text{O}_7$	60/308	2.5	63	Current work
$\text{Sn}_2\text{Mn}_2\text{O}_7$	41	5	41	[38]
$\text{Fe}_2\text{Mn}_2\text{O}_7$	68	5	63	[39]
$\text{Al}_2\text{Mn}_2\text{O}_7$	35	5	67	[40]
$\text{Ba}_2\text{FeMo}_{0.7}\text{V}_{0.3}\text{O}_6$	315	2.5	32	[33]

#### 4. Conclusions

In the prepared  $\text{La}_{1.4}\text{Sr}_{1.6}\text{Mn}_{2-x}\text{Nb}_x\text{O}_7$  series with varying Nb content ( $0.0 \leq x \leq 0.15$ ), the Nb content promoted a volumetric expansion in the unit cell of the R-P phase, due to its large ionic radii as compared to the Mn. This resulted in the separation of distinct structural phases alongside the R-P phase. Each Nb-modified sample represented two transition temperatures, one below 100 K (transition 1) and the other located above room temperature (transition 2). These transition points individually represented the magnetic

contribution of the structural phase for which the FM–PM transition in the low temperature region could be due to R-P phase, and  $T_C$  values towards room temperature may correspond to another perovskite phase. In addition, the incorporation of Nb in place of Mn replaces the long-range Mn–O–Mn double exchange ordering with short-range Mn–O–Nb, Nb–O–Nb magnetic interactions, and this led to the decrease in  $T_C$  and magnetization values. Among the Nb-doped compounds, the transition width of the first component decreased with an increase in the Nb concentration, while the contribution of the second component swiftly rose thereby symbolizing competition among the phase separated magnetic states. It was also validated in isothermal magnetization and  $\Delta S_M$  curves. Moreover, it was indicated that the ferromagnetic region of the competing second magnetic component coexisted within the main domain of the first component, collectively reflecting a ferromagnetic magnetization response within a broad temperature region. While the RC values of doped compounds were relatively smaller than those of the parent compound, it is noteworthy that the refrigerant capacity value obtained for the Nb-doped compounds remained consistent across a wide temperature range. The uniform refrigerant capacity, wide isothermal magnetic entropy change and second order magnetic transition over a broad temperature range are highly promising characteristics of these compounds to attain a good magnetocaloric performance.

**Author Contributions:** Conceptualization, A.K. and B.H.K.; Methodology, A.K.; Software, A.K. and M.K.S.; Validation, B.H.K.; Formal analysis, A.K., J.W.K., M.K.S., K.K., A.V. and B.H.K.; Investigation, M.K.S., K.K., A.V. and B.H.K.; Resources, B.H.K.; Data curation, A.K., M.K.S., K.K., A.V. and B.H.K.; Writing—original draft, A.K.; Writing—review & editing, A.K., J.W.K., M.K.S., K.K., A.V. and M.K.S., K.K., A.V. and B.H.K.; Visualization, J.W.K., M.K.S., K.K. and A.V.; Supervision, B.H.K.; Project administration, B.H.K.; Funding acquisition, B.H.K. All authors have read and agreed to the published version of the manuscript.

**Funding:** This research was funded by the financial program for self-directed research capacity in 2022, by Changwon National University, Republic of Korea.

**Institutional Review Board Statement:** Not Applicable.

**Informed Consent Statement:** Not Applicable.

**Data Availability Statement:** The raw data supporting the conclusions of this article will be made available by the authors on request.

**Acknowledgments:** This research was funded by the financial program for self-directed research capacity in 2022, by Changwon National University, Republic of Korea.

**Conflicts of Interest:** The authors declare no conflict of interest.

## References

1. Franco, V.; Blázquez, J.S.; Ingale, B.; Conde, A. The magnetocaloric effect and magnetic refrigeration near room temperature: Materials and models. *Annu. Rev. Mater. Res.* **2012**, *42*, 305–342. [[CrossRef](#)]
2. Gutfleisch, O.; Willard, M.A.; Brück, E.; Chen, C.H.; Sankar, S.G.; Liu, J.P. Magnetic Materials and Devices for the 21st Century: Stronger, Lighter, and More Energy Efficient. *Adv. Mater.* **2011**, *23*, 821–842. [[CrossRef](#)] [[PubMed](#)]
3. Gottschall, T.; Skokov, K.P.; Fries, M.; Taubel, A.; Radulov, I.; Scheibel, F.; Benke, D.; Riegg, S.; Gutfleisch, O. Magnetic Refrigeration: Making a Cool Choice: The Materials Library of Magnetic Refrigeration. *Adv. Energy Mater.* **2019**, *9*, 1970130. [[CrossRef](#)]
4. Ram, N.R.; Prakash, M.; Naresh, U.; Kumar, N.S.; Sarmash, T.S.; Subbarao, T.; Kumar, R.J.; Kumar, G.R.; Naidu, K.C.B. Review on Magnetocaloric Effect and Materials. *J. Supercond. Nov. Magn.* **2018**, *31*, 1971–1979. [[CrossRef](#)]
5. Salazar-Muñoz, V.E.; Guerrero, A.L.; Palomares-Sánchez, S.A. Review of magnetocaloric properties in lanthanum manganites. *J. Magn. Magn. Mater.* **2022**, *562*, 169787. [[CrossRef](#)]
6. Ferreira, M.C.; Pimentel, B.; Andrade, V.; Zverev, V.; Gimaev, R.R.; Pomorov, A.S.; Pyatakov, A.; Alekhina, Y.; Komlev, A.; Makarova, L.; et al. Understanding the Dependence of Nanoparticles Magnetothermal Properties on Their Size for Hyperthermia Applications: A Case Study for La–Sr Manganites. *Nanomaterials* **2021**, *11*, 1826. [[CrossRef](#)] [[PubMed](#)]
7. Anusree, V.K.; Ranjana, R.D.; Lekshmi, P.N.; Dhal, R.; Colin, C.V.; Santhosh, P.N. Giant exchange bias effect in Ruddlesden–Popper oxides  $\text{SrLaFe}_{0.25+x}\text{Mn}_{0.25}\text{Co}_{0.5-x}\text{O}_4$  ( $x = 0, 0.25$ ): Role of the cluster glass magnetic phase in a quasi-two-dimensional perovskite. *Phys. Rev. B* **2020**, *102*, 134405.

8. Elouafi, A.; Ounza, Y.; Omari, L.H.; Oubla, M.; Lassri, M.; Sajieddine, M.; Lassri, H. Spin-glass-like behavior and magnetocaloric properties in LaBiCaMn<sub>2</sub>O<sub>7</sub> layered perovskite. *Appl. Phys. A* **2021**, *127*, 216. [[CrossRef](#)]
9. Kumar, A.; Kumari, K.; Sharma, M.K.; Vij, A.; Kumar, S.; Huh, S.-H.; Koo, B.H. Chemically inducing room temperature spin-crossover in double layered magnetic refrigerants Pr<sub>1.4+x</sub>Sr<sub>1.6-x</sub>Mn<sub>2</sub>O<sub>7</sub> (0.0 ≤ x ≤ 0.5). *J. Mater. Sci. Technol.* **2022**, *124*, 232–242. [[CrossRef](#)]
10. Han, L.; Zhang, P.; Zhang, Y.; Zhu, H.; Liu, W.; Yang, J. Structure, magnetocaloric and critical properties of layered La<sub>2</sub>Sm<sub>0.4</sub>Sr<sub>0.6</sub>Mn<sub>2</sub>O<sub>7</sub> perovskite. *Ceram. Int.* **2017**, *43*, 8709–8714. [[CrossRef](#)]
11. M'nassri, R.; Nofal, M.M.P. de Rangoc and N. Chniba-Boudjada, Magnetic entropy table-like shape and enhancement of refrigerant capacity in La<sub>1.4</sub>Ca<sub>1.6</sub>Mn<sub>2</sub>O<sub>7</sub>-La<sub>1.3</sub>Eu<sub>0.1</sub>Ca<sub>1.6</sub>Mn<sub>2</sub>O<sub>7</sub> composite. *RSC Adv.* **2019**, *9*, 14916. [[CrossRef](#)] [[PubMed](#)]
12. Hassayoun, O.; Baazaoui, M.; Laouyenne, M.R.; Hosni, F.; Hlil, E.K.; Oumezzine, M.; Farah, K. Magnetocaloric effect and electron paramagnetic resonance studies of the transition from ferromagnetic to paramagnetic in La<sub>0.8</sub>Na<sub>0.2</sub>Mn<sub>1-x</sub>Ni<sub>x</sub>O<sub>3</sub> (0 ≤ x ≤ 0.06). *J. Phys. Chem. Solids* **2019**, *135*, 109058. [[CrossRef](#)]
13. Chihi, I.; Baazaoui, M.; Mahjoub, S.; Cheikhrouhou, W.; Oumezzine, M.; Farah, K. Study of the magnetic and magnetocaloric properties of new perovskite—Type materials: La<sub>0.6</sub>Ba<sub>0.2</sub>Sr<sub>0.2</sub>Mn<sub>1-x</sub>Fe<sub>x</sub>O<sub>3</sub>. *Appl. Phys. A* **2019**, *125*, 627. [[CrossRef](#)]
14. Phan, M.-H.; Phan, T.-L.; Yu, S.-C.; Tho, N.D.; Chau, N. Large magnetocaloric effect in La<sub>0.845</sub>Sr<sub>0.155</sub>Mn<sub>1-x</sub>M<sub>x</sub>O<sub>3</sub> (M = Mn, Cu, Co) perovskites. *Phys. Stat. Sol.* **2004**, *241*, 1744–1747. [[CrossRef](#)]
15. Wu, B.; Guo, D.; Wang, Y.; Zhang, Y. Crystal structure; magnetic properties, and magnetocaloric effect in B-site disordered RE<sub>2</sub>CrMnO<sub>6</sub> (RE = Ho and Er) perovskites. *Ceram. Int.* **2020**, *46*, 11988–11993. [[CrossRef](#)]
16. Selmi, A.; M'nassri, R.; Cheikhrouhou-Koubaa, W.; Boudjada, N.C.; Cheikhrouhou, A. The effect of Co doping on the magnetic and magnetocaloric properties of Pr<sub>0.7</sub>Ca<sub>0.3</sub>Mn<sub>1-x</sub>Co<sub>x</sub>O<sub>3</sub> manganites. *Ceram. Int.* **2015**, *41*, 7723–7728. [[CrossRef](#)]
17. Manoharan, S.S.; Singh, B.; Sahu, R.K. Powder neutron diffraction evidence for enhanced inter plane magnetic coupling in La<sub>1.2</sub>Sr<sub>1.8</sub>Mn<sub>2-x</sub>Ru<sub>x</sub>O<sub>7</sub> layered manganites. *J. Appl. Phys.* **2007**, *101*, 09G516. [[CrossRef](#)]
18. Karimunnesa, S.; Ahmmad, B.; Basith, M.A. Effect of strontium substitution on the structural and magnetic properties of La<sub>1.8</sub>Sr<sub>0.2</sub>MMnO<sub>6</sub> (M = Ni, Co)-layered manganites. *Phase Transit.* **2017**, *90*, 677–686. [[CrossRef](#)]
19. Swetha, K.; Bharadwaj, S.; Kumar, N.P.; Chelvane, J.A.; Lakshmi, Y.K. Above room temperature magnetic entropy in non-stoichiometric manganese of La<sub>0.67</sub>Sr<sub>0.33</sub>MnO<sub>3</sub> manganites. *Appl. Phys. A* **2022**, *128*, 727. [[CrossRef](#)]
20. Tozri, A.; Dhahri, E. Structural and magnetotransport properties of (La, Pr)-Ba manganites. *J. Alloys Compd.* **2019**, *783*, 718–728. [[CrossRef](#)]
21. Baazaoui, M.; Hcini, S.; Boudard, M.; Zemni, S.; Oumezzine, M. Critical behavior near the ferromagnetic–paramagnetic phase transition temperature of Pr<sub>0.67</sub>Ba<sub>0.33</sub>Mn<sub>1-x</sub>Fe<sub>x</sub>O<sub>3</sub> (x = 0 and 0.05) manganite. *J. Magn. Magn. Mater.* **2016**, *401*, 323–332. [[CrossRef](#)]
22. Guedri, A.; Mnefui, S.; Hcini, S.; Hlil, E.K.; Dhahri, A. B-site substitution impact on structural and magnetocaloric behavior of La<sub>0.55</sub>Pr<sub>0.1</sub>Sr<sub>0.35</sub>Mn<sub>1-x</sub>Ti<sub>x</sub>O<sub>3</sub> manganites. *J. Solid State Chem.* **2021**, *297*, 122046. [[CrossRef](#)]
23. Nanto, D.; Akbar, H.; Soegijono, B.; Kurniawan, B.; Ghosh, N.; Hwang, J.-S.; Yu, S.-C. Temperature span of magnetocaloric effect in Nb-doped La<sub>0.7</sub>Ca<sub>0.3</sub>Mn<sub>1-x</sub>Nb<sub>x</sub>O<sub>3</sub> (x = 0.000, 0.002 and 0.01). *Phys. B Condens. Matter* **2017**, *526*, 160–165. [[CrossRef](#)]
24. Arayedh, B.; Kallel, S.; Kallel, N.; Peña, O. Influence of non-magnetic and magnetic ions on the MagnetoCaloric properties of La<sub>0.7</sub>Sr<sub>0.3</sub>Mn<sub>0.9</sub>M<sub>0.1</sub>O<sub>3</sub> doped in the Mn sites by M=Cr, Sn, Ti. *J. Magn. Magn. Mater.* **2014**, *361*, 68–73. [[CrossRef](#)]
25. Fawcett, I.D.; Sunstrom, J.E.; Greenblatt, M.; Croft, M.; Ramanujachary, K.V. Structure, magnetism, and properties of Ruddlesden-Popper calcium manganates prepared from citrate gels. *Chem. Mater.* **1998**, *10*, 3643–3651. [[CrossRef](#)]
26. Saini, N.; Jindal, R.; Tripathi, A. Study of lattice dynamics of bilayered tetragonal Ruddlesden-Popper compounds (Ca, Sr)<sub>3</sub>Mn<sub>2</sub>O<sub>7</sub>. *Mater. Today Commun.* **2023**, *34*, 105190. [[CrossRef](#)]
27. Shannon, R.D. Revised effective ionic radii and systematic studies of interatomic distances in halides and chalcogenides. *Acta Cryst.* **1976**, *A32*, 751–767. [[CrossRef](#)]
28. Velikodnyi, Y.A.; Sirotinkin, V.P.; Trunov, V.K. The structure of the double pyrovanadate K<sub>2</sub> Mg V<sub>2</sub> O<sub>7</sub>. *Russ. J. Inorg. Chem. (Zhurnal Neorg. Khimii)* **1984**, *29*, 648–651.
29. Raju, K.; Song, M.S.; Lee, J.Y. Crystal structure and magnetic properties of La<sub>2-x</sub>(Sr<sub>0.5</sub>Ca<sub>0.5</sub>)<sub>1-x</sub>Mn<sub>2</sub>O<sub>7</sub> (x = 0.6, 0.8 and 1.0) Ruddlesden-Popper manganites. *J. Alloys Compd.* **2014**, *358–359*, 119–122. [[CrossRef](#)]
30. Li, H.F.; Su, Y.; Persson, J.; Meuffels, P.; Walter, J.M.; Skowronek, R.; Brückel, T. Neutron-diffraction study of structural transition and magnetic order in orthorhombic and rhombohedral La<sub>7/8</sub>Sr<sub>1/8</sub>Mn<sub>1-γ</sub>O<sub>3+δ</sub>. *J. Phys. Condens. Matter* **2007**, *19*, 176226. [[CrossRef](#)] [[PubMed](#)]
31. Koc, N.S.; Altintas, S.P.; Mahamdoua, N.; Terzioglu, C. Cation size mismatch effect in (La<sub>1-y</sub>RE<sub>y</sub>)<sub>1.4</sub>Ca<sub>1.6</sub>Mn<sub>2</sub>O<sub>7</sub> perovskite manganites. *J. Alloys Compd.* **2019**, *797*, 471–476.
32. Kumar, B.; Tiwari, J.K.; Chauhan, H.C.; Ghosh, S. Multiple magnetic phase transitions with different universality classes in bilayer La<sub>1.4</sub>Sr<sub>1.6</sub>Mn<sub>2</sub>O<sub>7</sub> manganite. *Sci. Rep.* **2021**, *11*, 21184. [[CrossRef](#)] [[PubMed](#)]
33. Hussain, I.; Kumar, A.; Khan, S.N.; Brojabasi, P.; Koo, B.H. Effect of B-site vanadium (V) doping on the structural, magnetic and magnetocaloric properties of Ba<sub>2</sub>FeMo<sub>1-x</sub>V<sub>x</sub>O<sub>6</sub> perovskite. *Solid State Commun.* **2020**, *310*, 113861. [[CrossRef](#)]
34. Banerjee, B.K. On a generalised approach to first and second order magnetic transitions. *Phys. Lett.* **1964**, *12*, 16–17. [[CrossRef](#)]
35. Smith, A.; Bahl, C.R.H.; Bjørk, R.; Engelbrecht, K.; Nielsen, K.K.; Pryds, N. Materials challenges for high performance magnetocaloric refrigeration devices. *Adv. Energy Mater.* **2012**, *2*, 1288–1318. [[CrossRef](#)]

36. Gschneidner, K.A., Jr.; Pecharsky, V.K.; Pecharsky, A.O.; Zimm, C.B. Recent Developments in Magnetic Refrigeration. *Mater. Sci. Forum* **1999**, *315–317*, 69–76.
37. Feng, J.Q.; Liu, Y.H.; Sui, J.H.; He, A.N.; Xia, W.X.; Wang, W.H.; Wang, J.Q.; Huo, J.T. Giant refrigerant capacity in Gd-based amorphous/nanocrystalline composite fibers. *Mater. Today Phys.* **2021**, *21*, 100528. [[CrossRef](#)]
38. Singh, K.; Rani, M.; Malik, V.K.; Panwar, N. Structural, Optical, Magnetic, and Magnetocaloric Properties of  $\text{Sn}_2\text{Mn}_2\text{O}_7$  Pyrochlore. *Phys. Status Solidi A* **2023**, *221*, 2300553. [[CrossRef](#)]
39. Khachnaoui, F.; Amor, N.B.; Bejar, M.; Dhahri, E.; Hlil, E.K. Synthesis and Magnetic Properties of New Pyrochlore  $\text{Fe}_2\text{Mn}_2\text{O}_7$  Compound. *J. Supercond. Nov. Magn.* **2018**, *31*, 3803–3808. [[CrossRef](#)]
40. Khachnaoui, F.; Amor, N.B.; Nouri, K.; Bejar, M.; Dhahri, E. Investigation of Griffiths-like phase at low temperature in a new magnetocaloric compound,  $\text{Al}_2\text{Mn}_2\text{O}_7$ . *J. Phys. Chem. Solids* **2021**, *148*, 109605. [[CrossRef](#)]

**Disclaimer/Publisher’s Note:** The statements, opinions and data contained in all publications are solely those of the individual author(s) and contributor(s) and not of MDPI and/or the editor(s). MDPI and/or the editor(s) disclaim responsibility for any injury to people or property resulting from any ideas, methods, instructions or products referred to in the content.